Supporting Information

Fitting Single Walled Carbon Nanotube Optical Spectra

Moritz Pfohl,[a,b] Daniel D. Tune,[a,c] Arko Graf,[d] Jana Zaumseil,[d] Ralph Krupke,[a,b] and Benjamin S. Flavel*[a].

[a] Institute of Nanotechnology, Karlsruhe Institute of Technology (KIT), P.O. Box 3640, 76021 Karlsruhe, Germany

[b] Institute of Materials Science, Technische Universität Darmstadt, Jovanka-Bontschits-Str. 2, 64287 Darmstadt, Germany

[c] Centre for Nanoscale Science and Technology, Flinders University, GPO Box 2100, 5042 Adelaide, Australia

[d] Institute for Physical Chemistry, Universität Heidelberg, Im Neuenheimer Feld 253, 69120 Heidelberg, Germany

Photoluminescence measurement

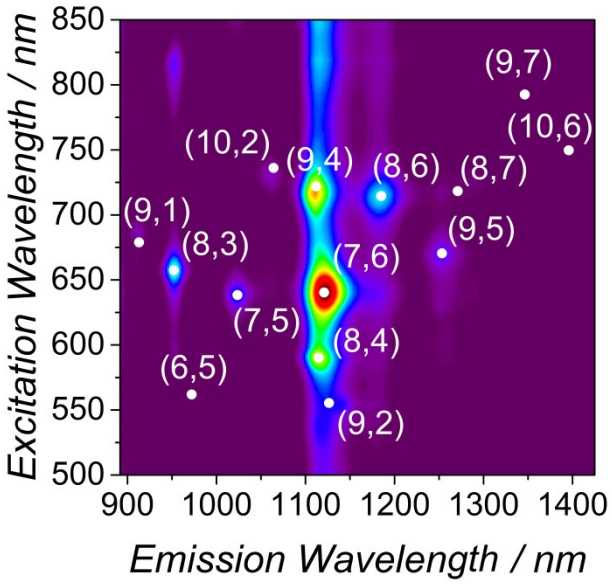

Figure S1. Photoluminescence contour plot of the polychiral suspension used to obtain the absorption spectra shown in Figure 1, Figure 2 and Figure 4. The position of the individual (n,m) species was calculated as outlined previously.[1-3]

(n,m) concentration for different background subtractions

Table S1. Spectral weight of different (n,m) species for different background subtraction methods.

	Spectral Weight (%)		
Background / SWCNT	k / λ^b (Nair et al.)	$Ae^{-b\lambda}$ (Naumov et al.)	Fano + Lorentzian (Tian et al.)
(7,6)	27.029	25.89	26.30
(8,6)	25.46	24.08	24.32
(9,5)	16.24	16.50	15.81
(7,5)	5.52	5.54	6.31
(8,3)	1.53	1.04	1.47
(9,1)	0.25	0.22	0.44
(6,5)	0.66	0.60	2.00
(10,2)	1.38	1.19	1.98
(9,4)	1.20	1.22	1.01
(8,4)	1.81	1.71	1.80
(9,2)	5.75	5.13	6.04
(8,7)	10.54	10.83	10.08
(9,7)	2.56	4.22	2.36
(10,6)	0.08	1.83	0.08

Gaussian and Lorentzian line shape

The Gaussian and Lorentzian line shapes can be defined based on their height or area as shown in eq S1 to S4. The relationship between area and height for Gaussian and Lorentzian line profiles can be determined by evaluating the area based function at the peak position λ_c, as demonstrated in eq S5 to S8:

$$y_{Gauss}(\lambda) = height \cdot e^{\left(-ln(2)\cdot\left(\frac{\lambda-\lambda_C}{0.5\cdot FWHM_G}\right)^2\right)} \quad \text{(S1)}$$

$$y_{Lorentz}(\lambda) = \frac{height}{1+\frac{\lambda-\lambda_C}{(0.5\cdot FWHM_L)^2}} \quad \text{(S2)}$$

$$y_{Gauss}(\lambda) = \sqrt{\frac{2\cdot ln(4)}{\pi}} \cdot \frac{area}{FWHM_G} \cdot e^{\left(-2\cdot ln(4)\cdot\left(\frac{\lambda-\lambda_C}{FWHM_G}\right)^2\right)} \quad \text{(S3)}$$

$$y_{Lorentz}(\lambda) = \frac{2\cdot area\cdot FWHM_L}{\pi} \cdot \frac{1}{4\cdot(\lambda-\lambda_c)^2+FWHM_L^2} \quad \text{(S4)}$$

$$y_{Gauss}(\lambda = \lambda_c) = height = \sqrt{\frac{2\cdot ln(4)}{\pi}} \cdot \frac{area}{FWHM_G} \cdot e^{\left(-2\cdot ln(4)\cdot\left(\frac{\lambda_C-\lambda_C}{FWHM_G}\right)^2\right)} \quad \text{(S5)}$$

$$height = \sqrt{\frac{2\cdot ln(4)}{\pi}} \cdot \frac{area}{FWHM_G} \quad \text{(S6)}$$

$$y_{Lorentz}(\lambda = \lambda_c) = height = \frac{2\cdot area\cdot FWHM_L}{\pi} \cdot \frac{1}{4\cdot(\lambda_c-\lambda_c)^2+FWHM_L^2} \quad \text{(S7)}$$

$$height = \frac{2\cdot area}{\pi\cdot FWHM_L} \quad \text{(S8)}$$

Derivation of Voigtian line-shape

The Voigtian function V(t) is defined as convolution[4] of a Gaussian (G) and Lorentzian (L) function:

$$V(t) = \int_{-\infty}^{+\infty} G(t')L(t-t')dt' \tag{S9}$$

In order to calculate the convolution integral, the Gaussian and Lorentzian functions are written as functions of "t" and "y" with t_c being the peak position:

$$G(y) = \sqrt{\frac{4\cdot ln(2)}{\pi}} \cdot \frac{e^{\left(-\frac{4\cdot ln(2)}{(FWHM_G)^2}\cdot y^2\right)}}{FWHM_G} \tag{S10}$$

$$L(t-y) = \frac{2\cdot area\cdot FWHM_L}{\pi} \cdot \frac{1}{4\cdot(t-t_c-y)^2+FWHM_L^2} \tag{S11}$$

The exponent of the Gaussian function can then be re-written as function of t':

$$\frac{4\cdot ln(2)}{(FWHM_G)^2}\cdot y^2 = (t')^2 \tag{S12}$$

$$y = \frac{t\prime\cdot FWHM_G}{\sqrt{4\cdot ln(2)}} \tag{S13}$$

Inserting the expression for y from eq S13 into the formalism of the Lorentzian function in eq S11 yields:

$$\begin{aligned} L(t-t') &= \frac{2\cdot area\cdot FWHM_L}{\pi}\cdot\frac{1}{4\cdot\left(t-t_c-\frac{t'\cdot FWHM_G}{\sqrt{4\cdot ln(2)}}\right)^2+FWHM_L^2} = \\ &= \frac{2\cdot area\cdot FWHM_L}{\pi}\cdot\frac{1}{4\cdot\left(\frac{\sqrt{4\cdot ln(2)}\cdot(t-t_c)-t'\cdot FWHM_G}{\sqrt{4\cdot ln(2)}}\right)^2+FWHM_L^2} = \\ &= \frac{2\cdot area\cdot FWHM_L}{\pi}\cdot\frac{1}{\frac{4\cdot FWHM_G{}^2}{4\cdot ln(2)}\cdot\left(\frac{\sqrt{4\cdot ln(2)}}{FWHM_G}\cdot(t-t_c)-t'\right)^2+FWHM_L^2} = \\ &= \frac{2\cdot area\cdot FWHM_L}{\pi}\cdot\frac{ln(2)}{FWHM_G{}^2}\cdot\frac{1}{\left(\frac{\sqrt{4\cdot ln(2)}}{FWHM_G}\cdot(t-t_c)-t'\right)^2+\frac{FWHM_L^2}{FWHM_G{}^2}\cdot ln(2)} \end{aligned} \tag{S14}$$

In the last step the differential dy has to be expressed as a function of dt', based on eq S13:

$$\frac{dy}{dt\prime} = \frac{FWHM_G}{\sqrt{4\cdot ln(2)}} \tag{S15}$$

$$dy = \frac{FWHM_G}{\sqrt{4\cdot ln(2)}}\cdot dt' \tag{S16}$$

Combining eq S12 with eq S10 and inserting it together with eq S14 and eq S16 into eq S9, the Voigtian function can be written in terms of its area:

$$V(t) = \int_{-\infty}^{+\infty} G(y)L(t-y)dy = \frac{FWHM_G}{\sqrt{4\cdot ln(2)}} \cdot \int_{-\infty}^{+\infty} G(t')L(t-t')dt' =$$

$$= \frac{FWHM_G}{\sqrt{4\cdot ln(2)}} \cdot \int_{-\infty}^{+\infty} \sqrt{\frac{4\cdot ln(2)}{\pi}} \cdot \frac{e^{(-(t')^2)}}{FWHM_G} \cdot \frac{2\cdot area\cdot FWHM_L}{\pi} \cdot \frac{ln(2)}{{FWHM_G}^2} \cdot \frac{1}{\left(\frac{\sqrt{4\cdot ln(2)}}{FWHM_G}\cdot(t-t_c)-t'\right)^2 + \frac{FWHM_L^2}{{FWHM_G}^2}\cdot ln(2)} =$$

$$= area \cdot \frac{2\cdot ln(2)\cdot FWHM_L}{\pi^{\frac{3}{2}}\cdot {FWHM_G}^2} \cdot \int_{-\infty}^{+\infty} \frac{e^{(-(t')^2)}}{\left(\frac{\sqrt{4\cdot ln(2)}}{FWHM_G}\cdot(t-t_c)-t'\right)^2 + \frac{FWHM_L^2}{{FWHM_G}^2}\cdot ln(2)} dt' \quad \text{(S17)}$$

Evaluating eq S17 at the peak position t_c yields:

$$V_{max}(t=t_c) = height = area \cdot \frac{2\cdot ln(2)\cdot FWHM_L}{\pi^{\frac{3}{2}}\cdot {FWHM_G}^2} \cdot \int_{-\infty}^{+\infty} \frac{e^{(-(t')^2)}}{\left(\frac{\sqrt{4\cdot ln(2)}}{FWHM_G}\cdot(t_c-t_c)-t'\right)^2 + \frac{FWHM_L^2}{{FWHM_G}^2}\cdot ln(2)} dt' =$$

$$= area \cdot \frac{2\cdot ln(2)\cdot FWHM_L}{\pi^{\frac{3}{2}}\cdot {FWHM_G}^2} \cdot \int_{-\infty}^{+\infty} \frac{e^{(-(t')^2)}}{(-t')^2 + \frac{FWHM_L^2}{{FWHM_G}^2}\cdot ln(2)} dt' \quad \text{(S18)}$$

A direct relation between peak height and area can then be proposed:

$$area \cdot \frac{2\cdot ln(2)\cdot FWHM_L}{\pi^{\frac{3}{2}}\cdot {FWHM_G}^2} = \frac{height}{\int_{-\infty}^{+\infty} \frac{e^{(-(t')^2)}}{(-t')^2 + \frac{FWHM_L^2}{{FWHM_G}^2}\cdot ln(2)} dt'} \quad \text{(S19)}$$

By applying the relationship given in eq S19 to eq S17, the Voigtian function can be expressed in terms of its height:

$$V(t) = height \cdot \frac{\int_{-\infty}^{+\infty} \frac{e^{(-(t')^2)}}{\left(\frac{\sqrt{4\cdot \ln(2)}}{FWHM_G}\cdot(t-t_c)-t'\right)^2 + \frac{FWHM_L^2}{{FWHM_G}^2}\cdot \ln(2)} dt'}{\int_{-\infty}^{+\infty} \frac{e^{(-(t')^2)}}{(-t')^2 + \frac{FWHM_L^2}{{FWHM_G}^2}\cdot \ln(2)} dt'} \quad \text{(S20)}$$

Deriving an expression for the Gaussian FWHM for Voigtian line-shsapes

The Voigtian FWHM was assumed to be constant (C_x, with x representing either the S_{11}, S_{22} or M_{11} region) in eV as per the work of Nair et al.[5] Based on eq S21 the FWHM was calculated in nm, with h being Planck's constant, c the speed of light and E_x the position of the peak absorption in the according region:

$$FWHM_V = \frac{C_x \cdot h \cdot c}{(E_x)^2 - \left(\frac{C_x}{2}\right)^2} \cdot 10^9 \tag{S21}$$

Olivero et al.[6] derived an analytical expression for the Voigtian FWHM:

$$FWHM_V = 0.5436 \cdot FWHM_L + \sqrt{0.2166 \cdot FWHM_L^2 + FWHM_G^2} \tag{S22}$$

Combining eq S21 and eq S22 it follows:

$$\frac{C_x \cdot h \cdot c}{(E_x)^2 - \left(\frac{C_x}{2}\right)^2} \cdot 10^9 = 0.5436 \cdot FWHM_L + \sqrt{0.2166 \cdot FWHM_L^2 + FWHM_G^2} \tag{S23}$$

The initial guess for the Lorentzian FWHM ($FWHM_L$) was calculated by assuming an equal contribution of Gaussian and Lorentzian FWHM to the Voigtian FWHM. Nevertheless, the supplied code offers the user the possibility to change this starting ratio (R) and the respective upper and lower boundaries of the ratio. However, all ratios are constrained to be within ± 20 % to be comparable; a constraint that can be changed to smaller or larger values by the user. The ratio is of Gaussian to Lorentzian FWHM is calculated by assuming the following:

$$\frac{FWHM_G}{FWHM_L} = R \tag{S24}$$

By resubstituting eq S24 into eq S23, it follows that:

$$\frac{C_x \cdot h \cdot c}{(E_x)^2 - \left(\frac{C_x}{2}\right)^2} \cdot 10^9 = 0.5436 \cdot FWHM_L + \sqrt{0.2166 \cdot FWHM_L^2 + FWHM_L^2 \cdot R^2} \tag{S25}$$

The Lorentzian FWHM can therefore be expressed as a function of E_{11} and R:

$$FWHM_L = \frac{C_x \cdot h \cdot c \cdot 10^9}{\left((E_x)^2 - \left(\frac{C_x}{2}\right)^2\right) \cdot \left(0.5436 + \sqrt{0.2166 + R^2}\right)} \tag{S26}$$

Voigtian and complex error function

The Voigtian function (in this case "K", to differentiate from the previous expression "V") represents the real part of the Faddeeva function (W) which, for y > 0, is identical to the complex error function (w):[7]

$$W(z) = K(x,y) + i \cdot L(x,y) = \frac{i}{\pi}\int_{-\infty}^{+\infty} \frac{e^{-t^2}}{z-t}\,dt \tag{S27}$$

$$w(z) = e^{-z^2}\left(1 + \frac{2i}{\sqrt{\pi}}\int_0^z e^{t^2}\,dt\right) = e^{-z^2}(1 - erf(-iz)) \tag{S28}$$

with the dimensionless variables x and y as defined in eq S29 and eq S30, respectively and z = x + i·y.

$$x = \sqrt{ln(2)} \cdot \frac{\lambda - \lambda_c}{HWHM_G} \tag{S29}$$

$$y = \sqrt{ln(2)} \cdot \frac{HWHM_L}{HWHM_G} \tag{S30}$$

The Voigt function K can be normalized to $\sqrt{\pi}$ and defined as shown in eq S31.

$$K(x,y) = \frac{y}{\pi}\int_{-\infty}^{+\infty} \frac{e^{-t^2}}{(x-t)^2+y^2}\,dt \tag{S31}$$

For a Voigtian line shape; instead of the FWHM, the half width at half maximum (HWHM) is used for calculation and can be expressed as a function of height and the real part of eq S28:

$$y_{Voigt} = height \cdot \frac{Re(w(x,y))}{Re(w(0,y))} \tag{S32}$$

Fitting procedure

For the fitting demonstrated in the present work, the initial peak positions of all line profiles were obtained from the databases provided by Bachilo et al.[2] for semiconducting (n,m) species (an alternative set of semiconducting nanotubes was provided by Weisman et al.[8]) and Nair et al.[5] for metallic nanotubes, and were allowed to vary between 0 and +20 nm. These boundary conditions were chosen under the assumption that the reference peak position resembles the case of the highest transition energies for each (n,m) species. As stated, upon bundling, a change in dielectric environment or the creation of defects, e.g. via sonication, the absorption peaks tend to red-shift because of an increased dielectric screening and exciton tunneling.[9-10] A different pair of boundary conditions for the allowed peak shift was assumed in the case where a peak in the measured spectrum was manually assigned to an (n,m) species (i.e. a spectral feature was enforced to be a certain nanotube type). In this case, the allowed red/blue shift was set to ±5 nm of the peak position identified in the spectra.

The FWHM of the EPS was assumed to vary between 50 – 200 % of its initial value during the fit. The FWHM is always calculated for the (n,m) species with the largest EPS and the FWHM of all subsequent (n,m) species is allowed to deviate from this value by ±10 % to enforce a similar line shape amongst all the EPSs fitted to a sample. The peak area was modeled based on the spectral weight transfer from a peak, S_x (I_{S_x}) with x=11 or x=22, to its corresponding EPS (I_{EPS}), as described by Perebeinos et al. with an additional, diameter independent factor f_1 as introduced in our previous work:[1, 11]

$$\frac{I_{EPS}}{I_{S_x}} = 0.017 + \frac{0.1\,nm}{d_t} + f_1 \qquad \text{(S33)}$$

The factor f_1 was allowed to vary during the fit between -0.07 and +0.07 to account for a marginally reduced or increased spectral weight transfer from S_x to the EPS.

Comparison of different FWHM starting values

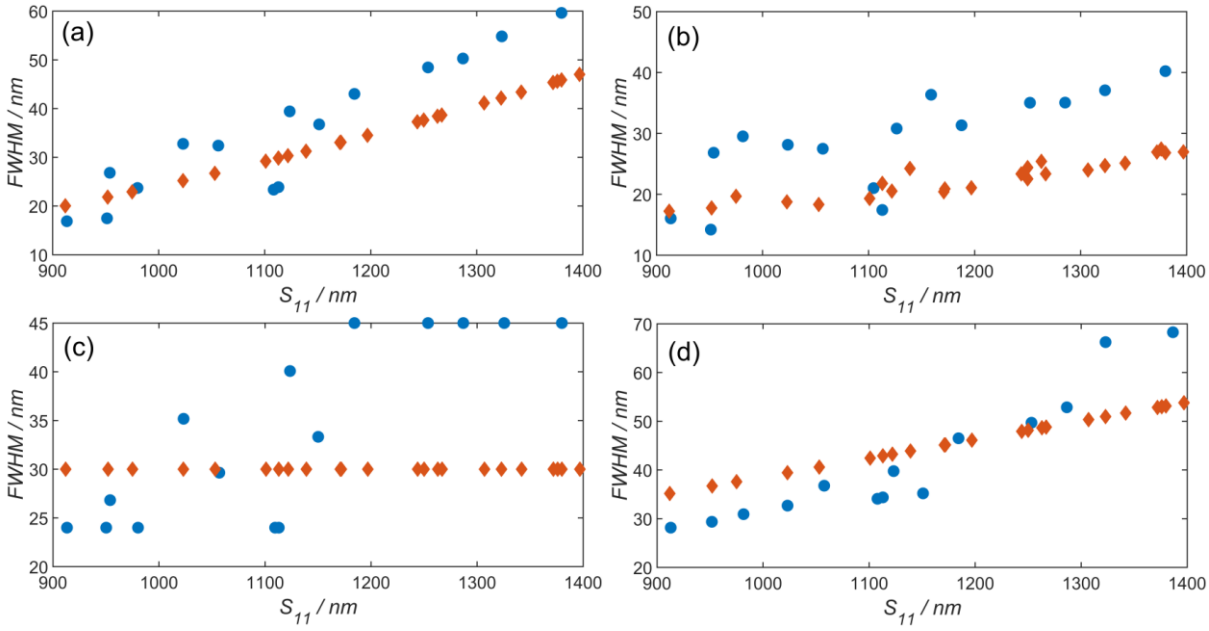

Figure S2. Comparison of FWHM starting values (red diamonds) and fitted values (blue circles) for different methods of estimating the initial FWHM for the nanotube suspension used in the main text: (a) constant FWHM in energy space,[5] (b) diameter dependent in frequency space,[12] (c) constant in nanometer and (d) as function of E_{11} in energy space.[13] The FWHM for (b) and (c) was allowed to vary within 80 to 150 % of its initial starting value as compared to (a) and (d) where it was allowed to vary between 80 and 130 % of its initial value. Based on the nSSE value, method (a) provides the best fit for this particular nanotube suspension with $4.33 \cdot 10^{-4}$, compared to $1.0 \cdot 10^{-2}$, $5.60 \cdot 10^{-4}$ and $7.1 \cdot 10^{-4}$ for (b) to (d).

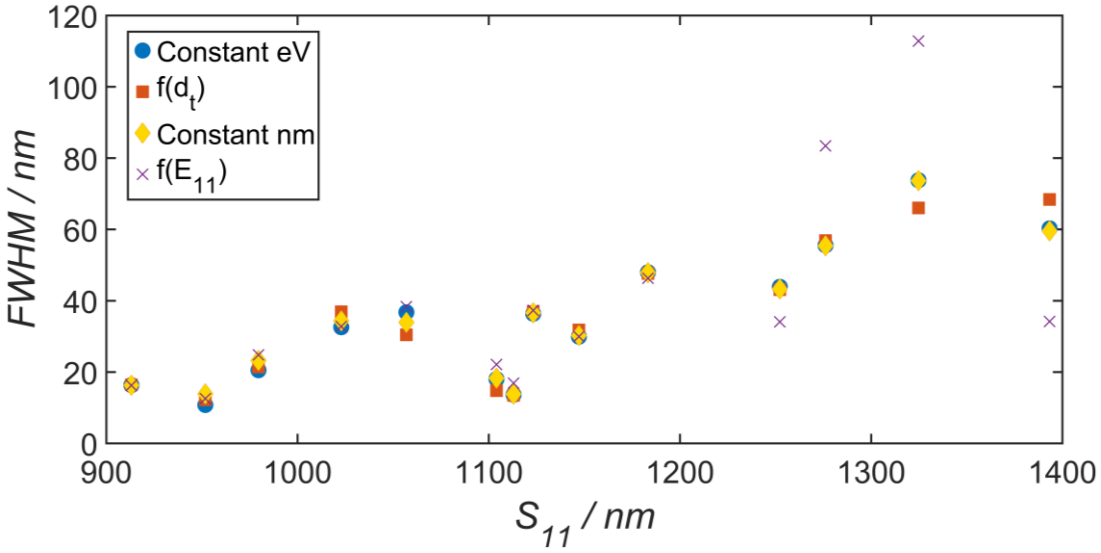

Figure S3. Fitted FWHM values using the four different methods of initial FWHM estimation, shown in Figure S2, where the FWHM is allowed to vary freely. Blue dots represent the method with a fixed FWHM in energy space,[5] red squares were calculated based on the nanotubes diameter,[12] yellow diamonds represent a constant FWHM in nm and purple crosses were initially calculated based on a linear function of the E_{11} absorption position.[13] Here it can be seen, that the FWHM obtained is the same, irrespective of the starting position. Nevertheless, good starting values allow for a more constrained and faster fit.

Importance of EPS

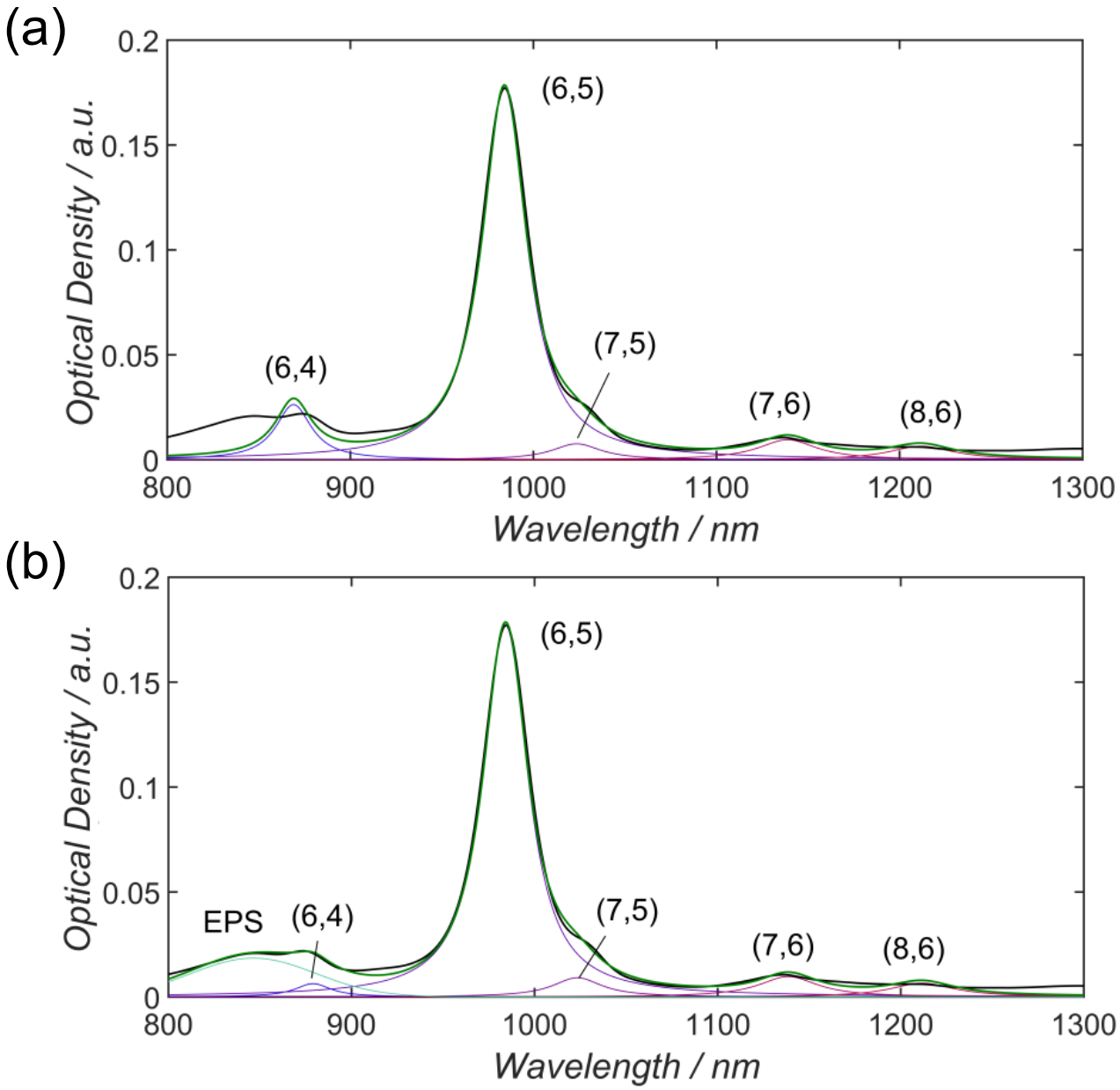

Figure S4. Fit of (6,5) enriched SWCNT solution (black) without (a) and with (b) an associated exciton-phonon sideband (EPS). The quality of the fit between 800 – 900 nm is improved by inclusion of an EPS for (6,5).

Alternative method for height assignment

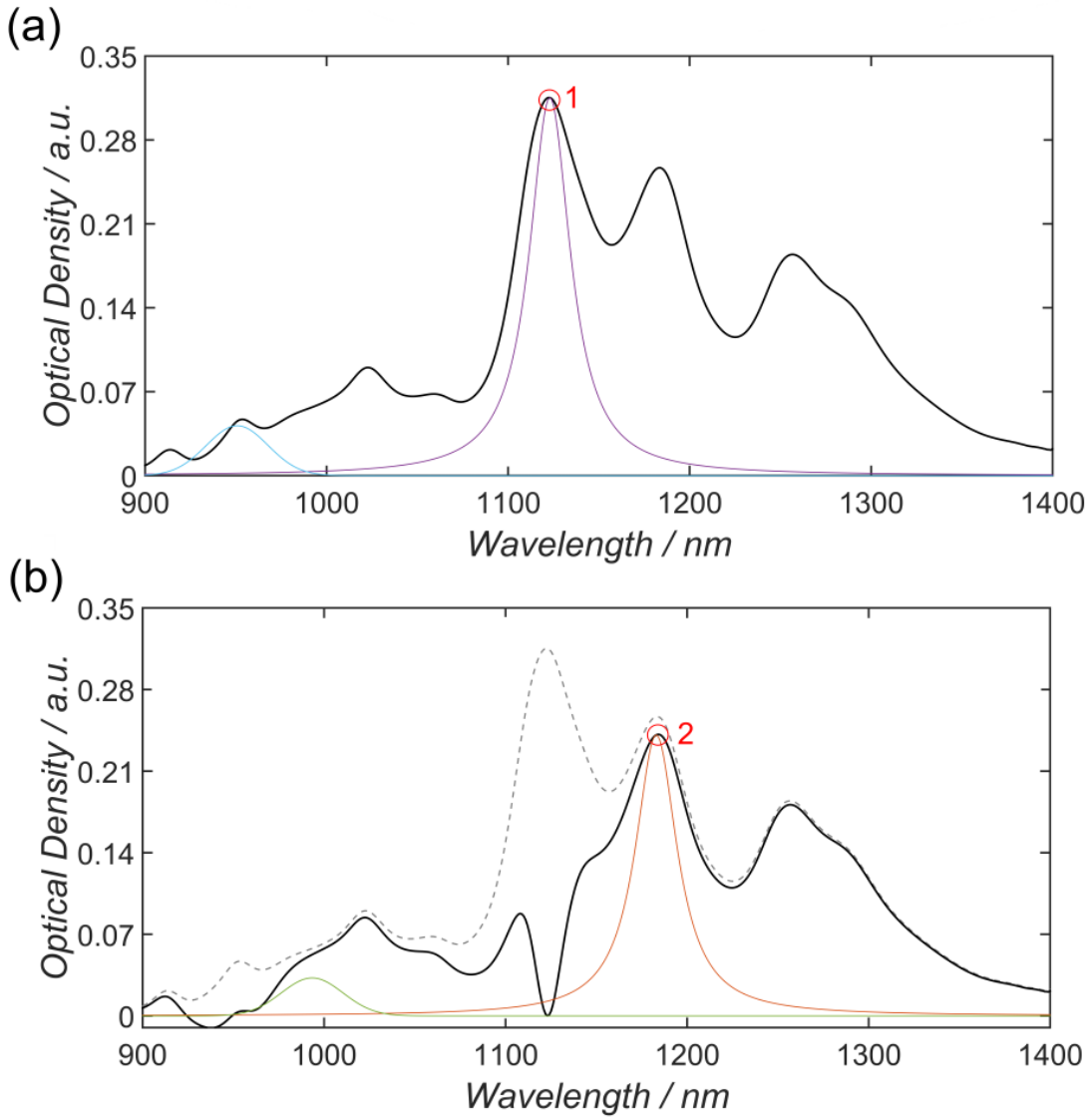

Figure S5. The method shown in (a) and (b) and is based on the sequential subtraction of ab initio calculated line profiles. In this routine, the largest peak (labeled 1) is considered first and both the line profile of the nanotube and any associated EPS are subtracted from the original spectrum to yield a "corrected" absorption spectrum. From this corrected spectrum, the second most intense nanotube peak (labeled 2) is calculated and again subtracted to yield a new corrected spectrum. This procedure is repeated for all (n,m) species under consideration and the height of the individual (n,m) species is varied between 10 and 120 % of the peak intensity in the corrected spectrum. This approach is well suited for monochiral or (n,m) enriched SWCNT absorption spectra with clearly separated peaks and minor contributions from low concentration (n,m) species. Another approach would be the combination of the method presented in Figure 2 and Figure S5 applied to the right and left, respectively, of a cut-off wavelength. However, it is possible to set this boundary condition to suitably high or low values such that the entire spectrum of interest is fitted with either of the methods shown in Figure 2 and Figure S5.

Voigtian, Lorentzian and Gaussian line profiles

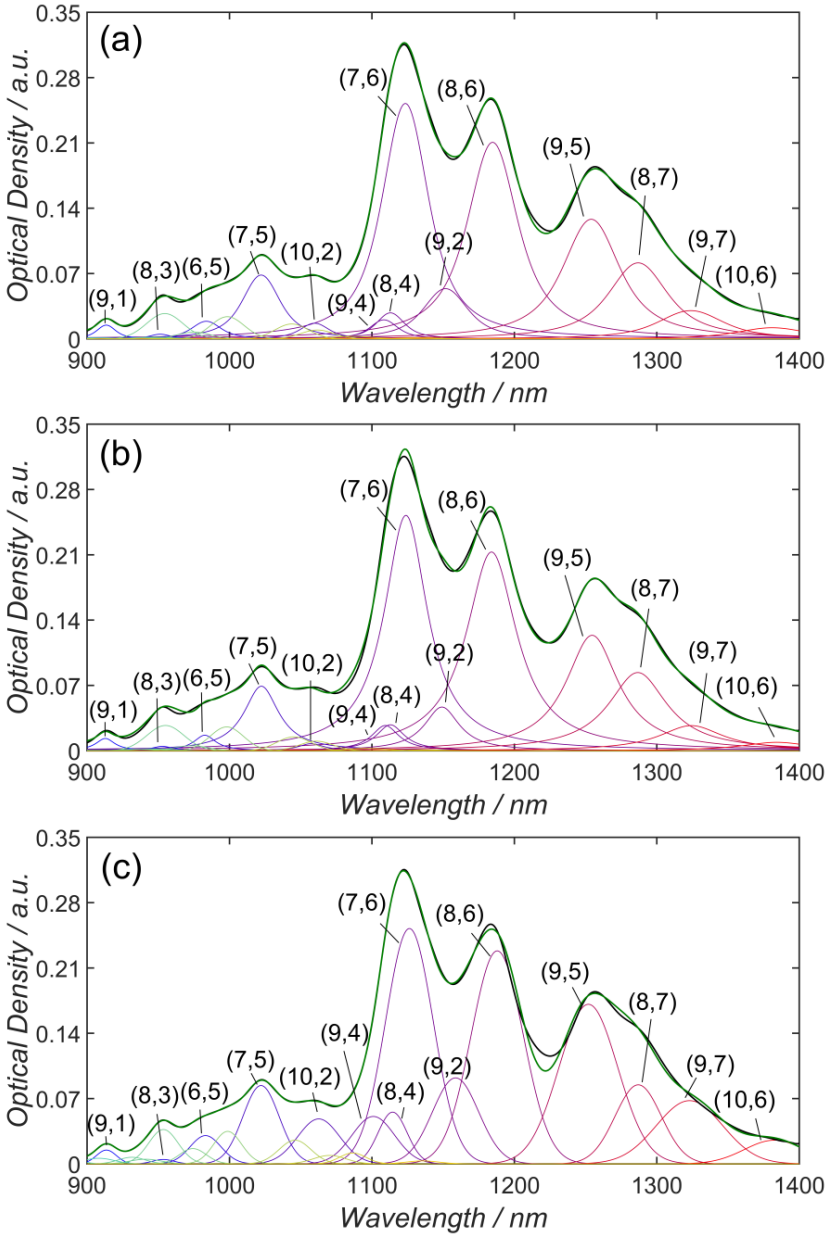

Figure S6. (a) Fit of the polychiral SWCNT solution (black) shown in Figure 1 with Voigtian line profiles (calculated spectra is shown in green and a background based on Naumov et al.[14] was subtracted). (b) and (c) The same polychiral nanotube solution fitted with Lorentzian and Gaussian line profiles, respectively. The difference in (n,m) distribution is visible, e.g. by comparing the shape of (7,6) and (8,6) or the calculated spectrum above 1200 nm where the contribution of (9,5) and (9,7) vary significantly for Gaussian line profiles compared to the other two line shapes. Peaks that were not assigned to any nanotube are exciton phonon sidebands.

Voigtian, Lorentzian and Gaussian line profiles were used to fit the polychiral nanotube solution shown in Figure 1. Comparing the normalized sum of squared errors (nSSE) value of these fits ($4.33 \cdot 10^{-4}$, $1.05 \cdot 10^{-3}$ and $2.22 \cdot 10^{-3}$, respectively) the Voigtian and Lorentzian line profiles seem to be best suited for fitting aqueous dispersions of polychiral SWCNTs.

Decongestion of different mixtures with known ratios

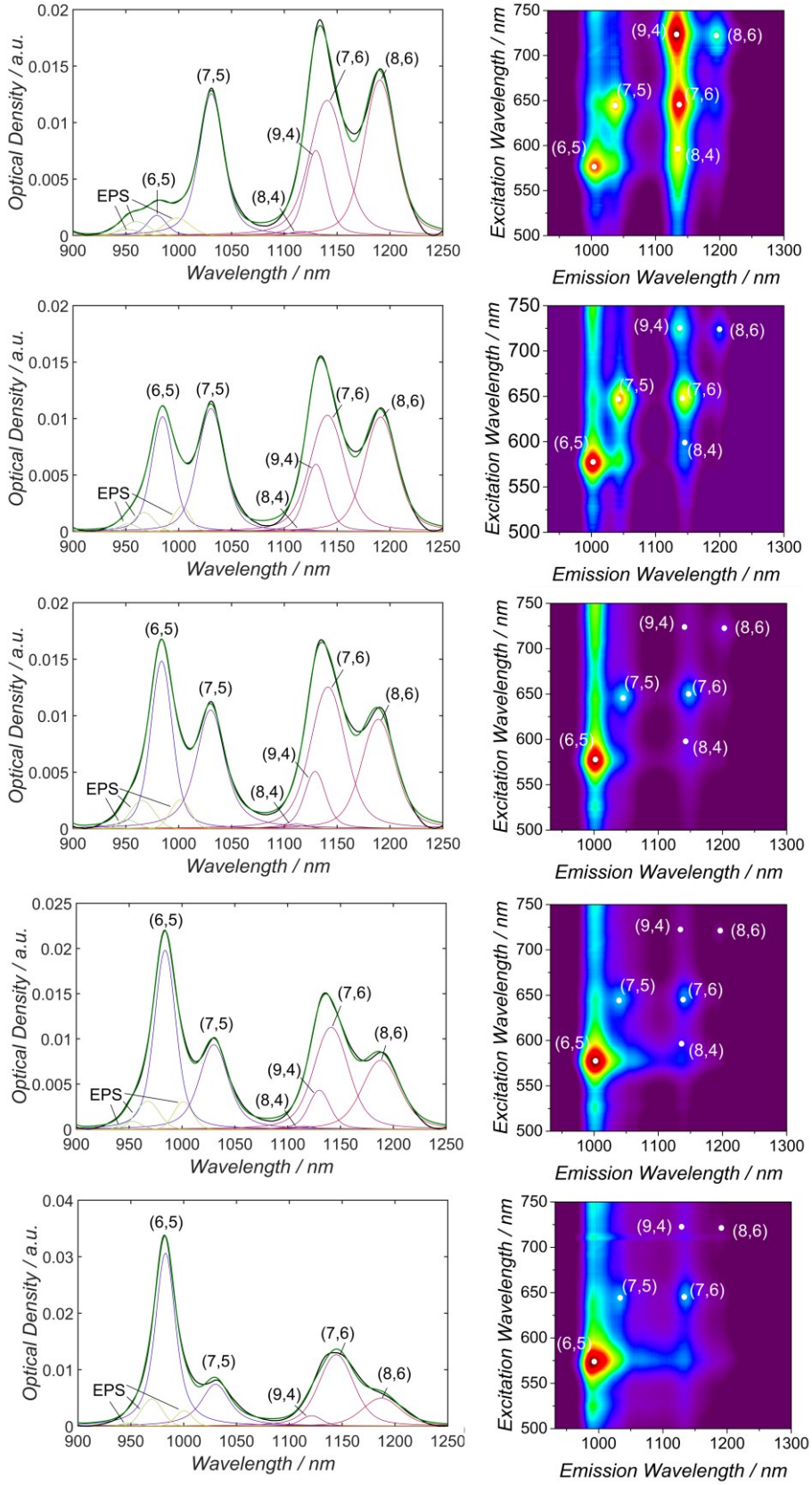

Figure S7. In the left column the optical absorption data of solution 1 (bottom), solution 2 (top) and mixtures thereof in ratios of 2:1, 1:2 and 1:2 (from bottom to top) are shown. In the right column, the corresponding PL measurements are shown.

Calculating the concentration of (6,5) and (7,5) in solution 1 and 2, the expected concentration ratio can be calculated according to the following equation, where r1 is the ratio taken of solution 1 and r2 the ratio of solution 2:

$$Concentration\ Ratio = \frac{r1 \cdot conc_{65_{sol1}} + r2 \cdot conc_{65_{sol2}}}{r1 \cdot conc_{75_{sol1}} + r2 \cdot conc_{75_{sol2}}} \quad \text{(S34)}$$

The fitted concentration ratio can be determined from Figure S7 by determining the concentration based on the optical density OD, cuvette path length l_{path} of 2 mm and the molar absorptivity ε calculated based on Sanchez et al.[15] for the different (n,m) species:

$$conc = \frac{OD}{l_{path} \cdot \varepsilon} \quad \text{(S35)}$$

The relative error between the measured concentration ratio in Figure S8 and the calculated one based on eq S34 was calculated to be 10.8 ± 2.5 %.

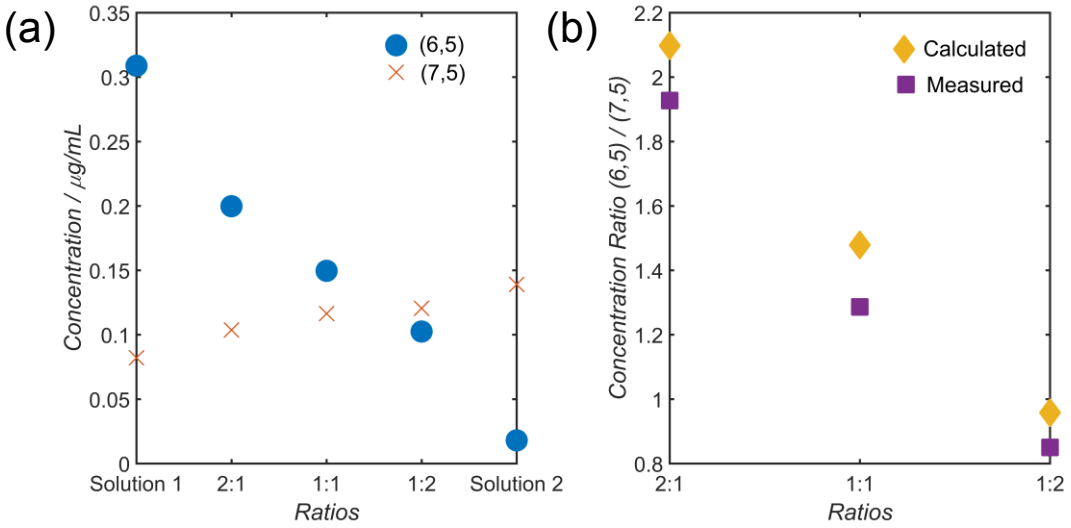

Figure S8. The concentration of (6,5) and (7,5) in solution 1, solution 2 and different ratios thereof are shown in (a). The measured and calculated concentration ratio for different mixtures is shown in (b).

Polychiral suspensions for comparison of (n,m) abundance

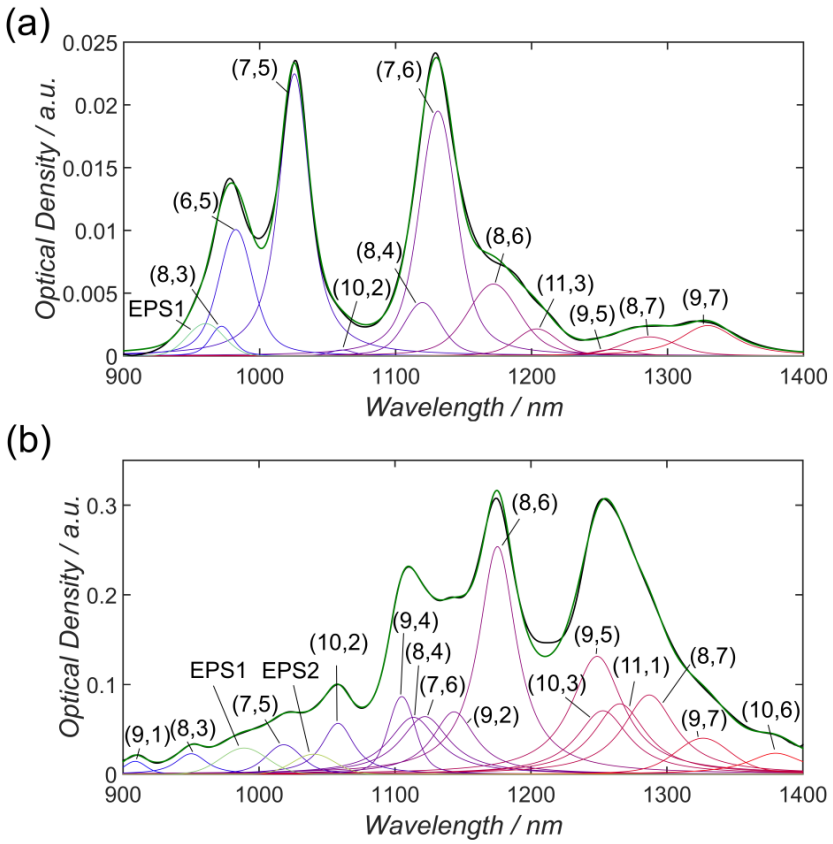

Figure S9. Comparison of two different polychiral solutions (a and b). The background corrected spectrum (with the method presented by Naumov et al.[14]) is shown in black while the calculated spectrum is shown in green. Along with the different (n,m) species (using Voigtian line profiles), the exciton phonon sidebands (EPSs) were also considered during fitting.

Fit of polymer sorted (6,5)

Polymer sorted (6,5) solutions were fitted in the S_{11} region with three different line profiles: Gaussian (Figure S10 (a)), Lorentzian (Figure S10 (c)) and Voigtian (Figure S10 (e)). Based on the S_{11} fit, the S_{22} region was fitted (Figure S10 right column). Upon comparing the region around 600 nm for Lorentzian and Voigtian fits ((d) and (f)), it seems as if (6,4) is missing. Having a closer look at the wavelength regime from 700 to 800 nm, S_{22} of (10,2) needs be included for Lorentzian and Voigtian fits.

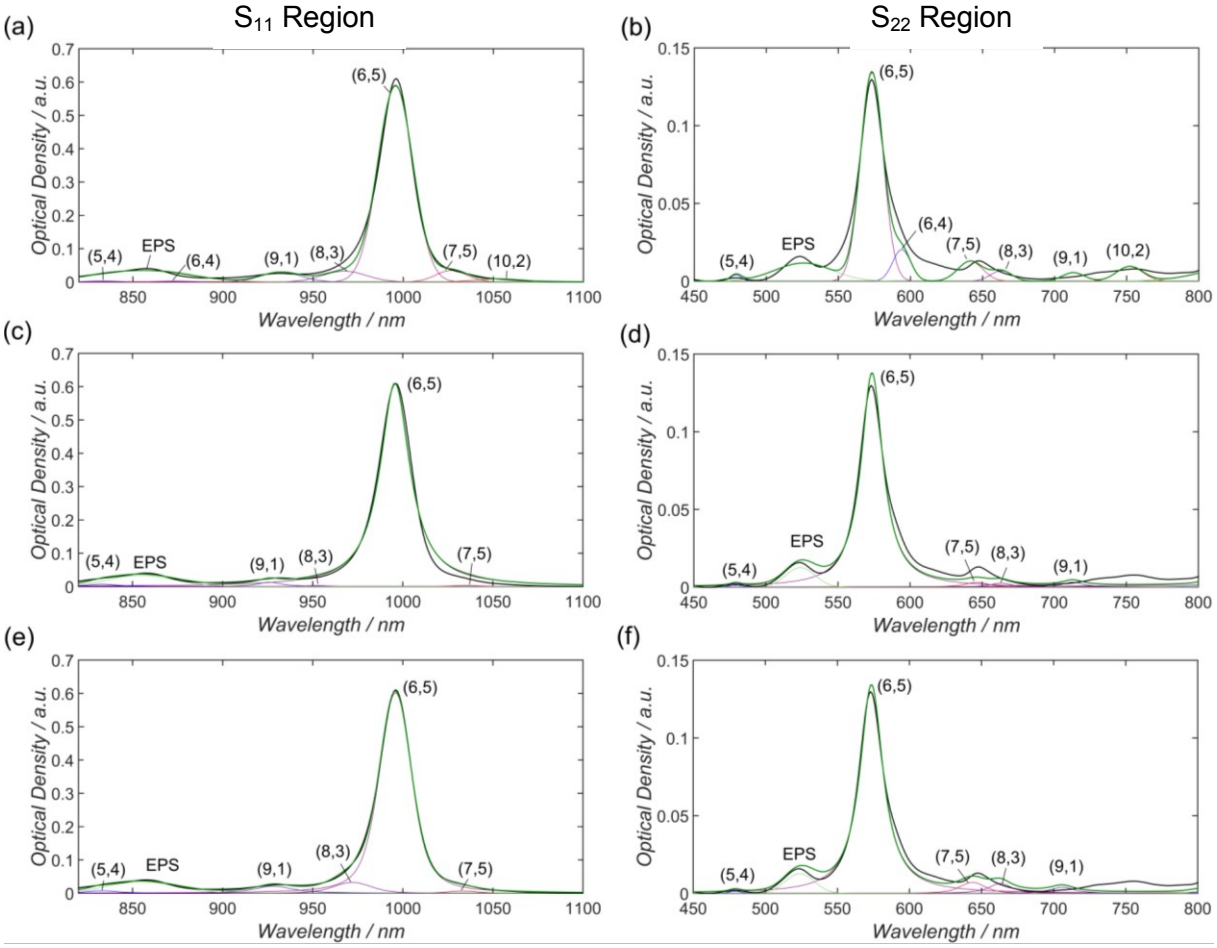

Figure S10. (a) Gaussian, (c) Lorentzian and (e) Voigtian line profiles were used to fit the nearly monochiral (6,5) solution (black) in the S_{11} region. The calculated spectrum is shown in green with nSSE values of 4.02×10^{-3}, 7.98×10^{-3} and 6.48×10^{-4} for Gaussian, Lorentzian and Voigtian fits, respectively. Based on this fit the S_{22} region was fitted (b), (d) and (f). The nSSE values for the entire region were calculated to be 7.52×10^{-3}, 8.97×10^{-3} and 2.19×10^{-3} for Gaussian, Lorentzian and Voigtian profiles, respectively. For monochiral, polymer sorted SWCNT solutions Gaussian and Voigtian line profiles seem to be the best choice for fitting the absorption spectrum.

Fitting results

The fitting results of the solution absorption measurement shown in Figure 4 are listed in full detail in Table S2.

Table S2. Fitting results for different (n,m) species in their S_{11} (left column) S_{22} (right column) and M_{11} transition region.

SWCNT	Center (nm)		FWHM (nm)		Area		Spectral Weight (%)	
(7,6)	1125	652	38.80	26.36	15.10	3.89	26.88	25.82
(8,6)	1184	723	43.01	31.44	14.19	4.12	25.27	27.33
(9,5)	1254	676	46.39	28.10	8.40	1.63	14.95	10.82
(7,5)	1022	641	31.76	13.29	2.94	0.39	5.24	2.62
(10,2)	1057	745	25.80	31.76	0.51	0.29	0.90	1.92
(8,3)	953	668	17.48	21.12	0.13	0.05	0.24	0.36
(9,1)	914	688	16.05	23.04	0.18	0.09	0.32	0.62
(6,5)	983	577	21.01	18.91	0.46	0.18	0.82	1.23
(9,4)	1110	723	23.36	27.36	0.57	0.30	1.02	1.98
(8,4)	1113	588	24.00	20.14	1.63	0.65	2.89	4.31
(9,2)	1151	564	28.22	17.62	1.59	0.32	2.84	2.13
(8,7)	1284	737	50.18	32.88	6.64	1.95	11.82	12.93
(9,7)	1323	801	54.38	39.11	2.75	0.94	4.89	6.23
(10,6)	1383	761	58.09	35.83	0.88	0.26	1.57	1.71
(7,7)	510		11.80		$48.15 \cdot 10^{-3}$		0.086	
(8,5)	512		12.09		$19.51 \cdot 10^{-3}$		0.035	
(12,3)	608		24.34		0.14		0.25	

In Table 2 it can be seen that there are large variations in the FWHM, especially for (8,6), (9,5), (9,7) which are much larger than (8,3) or (9,1). This can be a result of starting values that wandered far astray from the 'correct' values or are an indication of missing (n,m) species in the fit. In our work we have used PL measurements to quantitatively determine the (n,m) species to be fitted and constrained the fit accordingly. For some users this might be an acceptable approach but will require the user to accept that some FWHM values might be

significantly different to others. Alternatively, not seeing (n,m) species in PL is not necessarily confirmation that they do not exist in suspension and additional (n,m) species can be included in spectral regions with dramatically different FWHM values. In Figure S11 the same data has been fitted once again without constraining the (n,m) distribution by those species seen in PL. The reference data set extracted from Bachilo et al.[2] and a variation of the FWHM of ± 10 % was used. In this case the fitted FWHM follows to estimated FWHM trend closely, regardless of the initial estimation method used. However, once again for the suspension used in this analysis a fit based on a fixed FWHM in energy space is best.

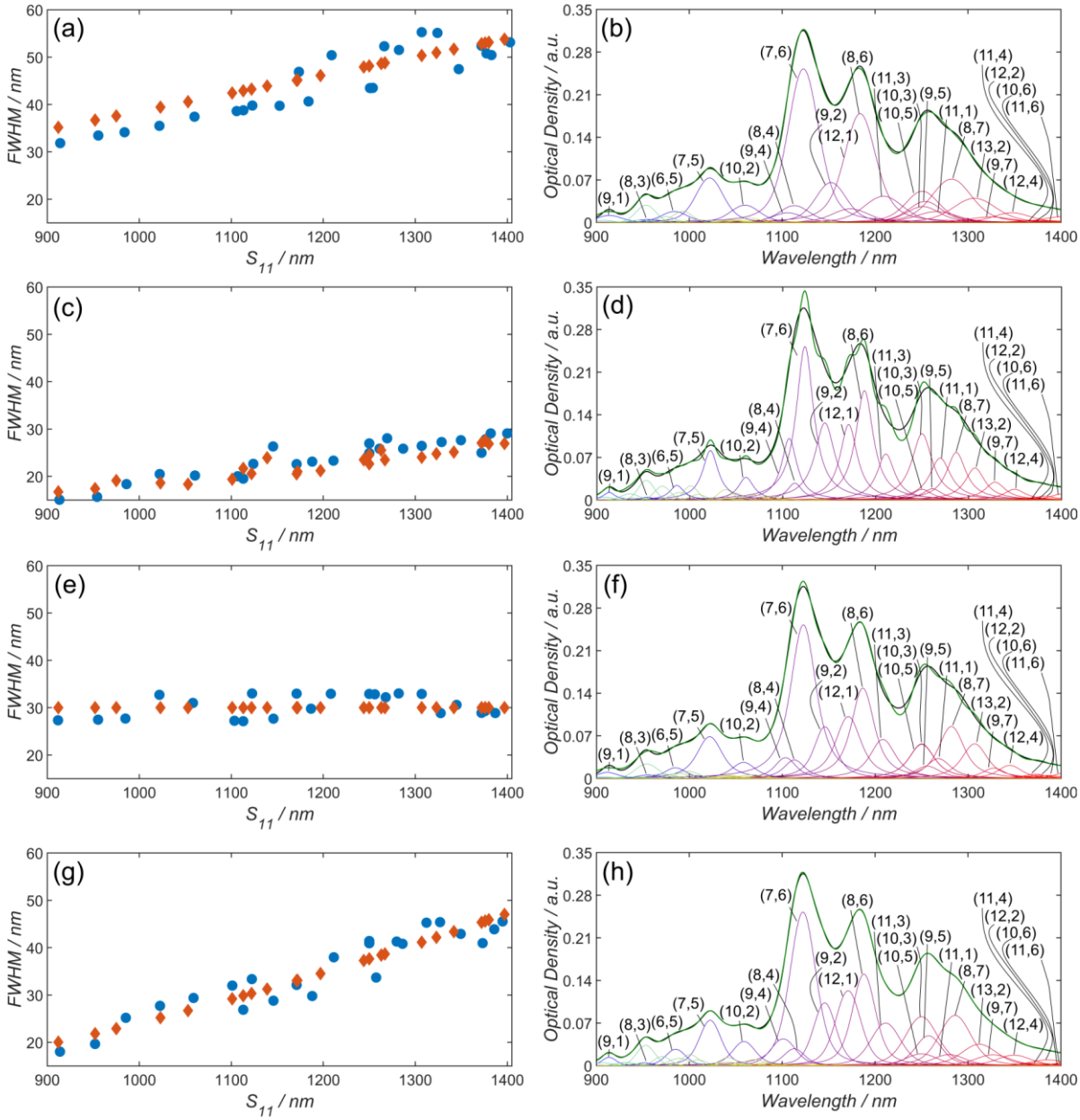

Figure S11. Consideration of all (n,m) species provided by Bachilo et al.,[2] with a variation of the initial starting value for the FWHM of ± 10 %. The best fit was obtained for a FWHM constant in eV (g and h)[5] with a nSSE of $1.02 \cdot 10^{-4}$. Increasing nSSE values were obtained for fits based on FWHM calculated as a function of E_{11} (a and b),[13] a constant FWHM of 30 nm (e and f) and a diameter dependent FWHM (c and d)[12] with $6.33 \cdot 10^{-4}$, $1.73 \cdot 10^{-3}$ and $7.69 \cdot 10^{-3}$, respectively.

Constrained fitting of film spectra

Beyond spectroscopic characterization, SWCNTs are rarely used in solution but are rather incorporated into solid films, composites, fibers, etc. Upon forming a film of carbon nanotubes, the optical properties of the SWCNTs are commonly observed to red shift, the peaks become broader, and the contribution of scattering to the background as a result of bundling is significantly increased compared to solution absorption measurements.[16-17] These effects result in greater spectral overlap which in turn increases the difficulty in accurately determining the (n,m) distribution within the film. Fitting film spectra of monochiral or chirality enriched SWCNTs can be straightforward as demonstrated by Berciaud et al.,[18] who used Lorentzian line profiles. For fitting polychiral film spectra, Tian et al. used Gaussian line profiles in their earlier work and Lorentzian line profiles in their later work, and assumed a constant FWHM (in eV).[19-20] In combination with the aforementioned set of two norm equations, they obtained a set of linear equations that were easy to solve and then they verified the results of their fit using transmission electron microscopy (TEM). Since the formation of a solid film necessarily involves the filtration, deposition, capture, or otherwise extraction of nanotubes from a solution, a straightforward and reliable way of fitting a film spectrum is to constrain the spectral weights of each nanotube in the film fit to be very close to those determined from a fit of the solution that was used to fabricate the film. Hereby, the total area under the corresponding spectral region for the film ($area_{total,Film}$) is calculated using numerical integration and then multiplied by the concentration of each (n,m) species in solution to yield its corresponding area in the film using eq S36:

$$area_{i,Film} = area_{total,Film} \cdot c_{i,Solution} \cdot x_i \tag{S36}$$

In the examples which follow, the concentration was allowed to vary between ±10 %, with x_i being the correction factor for the concentration. Additionally, a maximum red-shift of each nanotube's peak position must be introduced, and can be varied depending on the expected shift. For example, an allowed peak shift of 0 – 40 nm for surfactant wrapped SWCNTs is in agreement with previous reports in the literature,[16] however, for polymer wrapped SWCNTs this value should be significantly smaller.[21] The FWHM of the nanotube peaks was allowed to broaden during fitting between a factor of 1 to 2.5 to account for nanotube bundling but the broadening factor was constrained to be the same for all nanotubes. Furthermore the EPS was allowed to broaden by a factor of 1 - 3 and was also constrained to be the same for all exciton phonon sidebands. The correction factor f_l (eq S33) between (n,m) species was allowed to vary between -0.05 and 0.1 in agreement with our previous work.[1]

As stated for solution spectra and in accordance with Meier,[22] the shape of the background has a huge impact on the calculation of the absorption spectra. For film measurements on glass it is fairly easy to extend the measurement range beyond 1400 nm and therefore increase the long wavelength accuracy of the background correction methods of Tian et al. and Nair et al.[5, 19] Being able to constrain the fit based on a previous solution spectra and setting the change of the concentration to a reasonably small number therefore has two advantages: first, the fit of the film resembles the (n,m) distribution that was measured in solution previously. An example is provided in Figure S12, where a Fano and Lorentzian shaped background results in the best fit using the (n,m) distribution determined from Figure 1 (d). Second, a bad agreement of measured and calculated film absorption spectra might be caused by an insufficient background correction and be corrected by the choice of a different background.

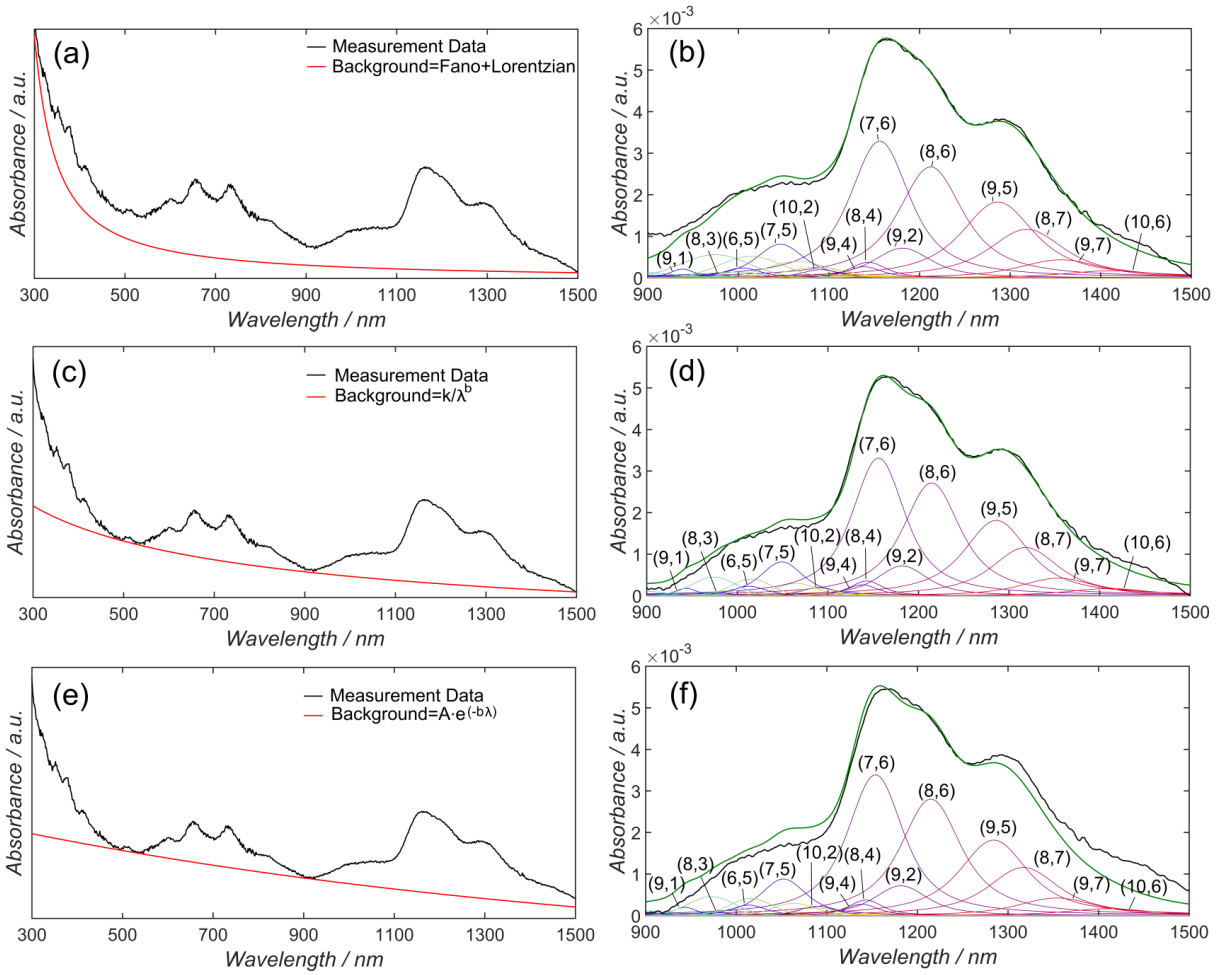

Figure S12. The measured film absorption spectrum is shown in black and the different background subtraction methods in the left column (a, c and e) in red. In the right column, the calculated spectrum of the film is shown in green (b, d and f). The film fit is constrained by the solution fit shown in Figure 1 (d) by a relative (n,m) distribution change of ±10 %.

Although it is possible to improve the quality of the fit for these approaches, this would require an unreasonable increase of the relative concentration change. An example is shown in Figure S13, where the relative concentration of each (n,m) species was allowed to vary ±100 % compared to the spectral concentration in solution. The effect of this improved fit quality on the spectral (n,m) concentrations in solution and film can also be seen in Table S3. In the case of Nair et al. (k/λ^b), a reduction in the concentration of (8,3) and (9,1) is apparent while for a background shape based on the work of Naumov et al. ($A \cdot e^{-\lambda \cdot b}$) the concentration of (6,5) is also drastically reduced and the spectral amounts of (9,7) and (10,6) are doubled. While small changes in the spectral area of species can occur due to (n,m) dependent differences in how the absorption properties alter during the bundling that occurs during film formation, or due to the absence of solvent, changes of ±100 % are most likely unphysical. This should be taken into account when adjusting parameters to obtain the best overall fit, and is one of the advantages of using the solution measurement to constrain the film fit.

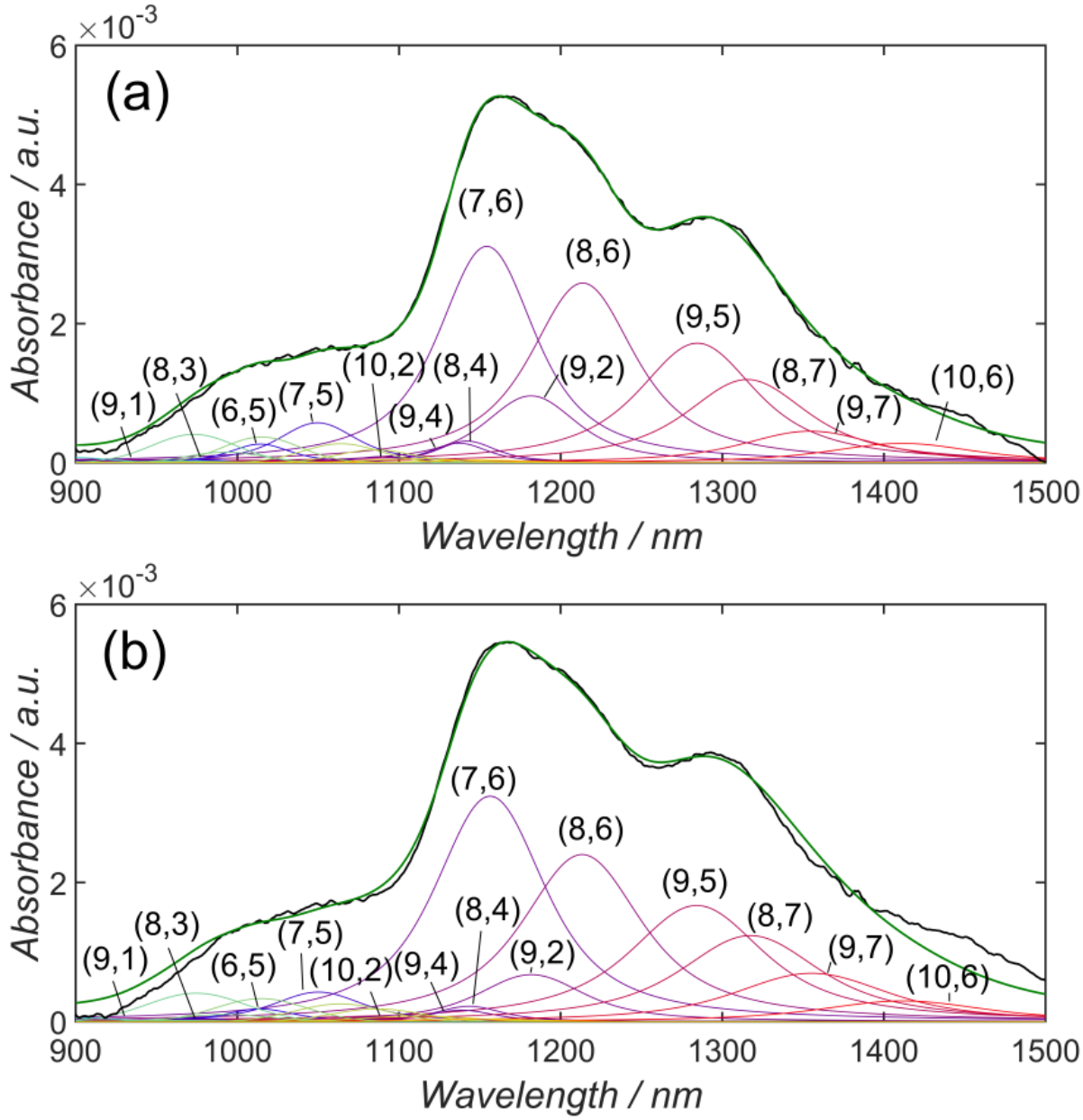

Figure S13. Film absorption measurement (black) and calculated spectrum (green) for the background subtraction approaches of Nair et al. (a) and Naumov et al. (b) where the relative concentration change was set to vary within $x_i = \pm 100\%$.

The fitting of a film or solid spectrum may seem to be of little use when the spectral concentrations of nanotubes in the solution that was used to create it are already known. However, it becomes particularly important in the cases where the film is treated with some agent, or deposited on some material, that is also optically active (e.g., dyes, fluorescent markers, quantum dots, etc.), or when the embedding matrix is itself optically active (e.g., some polymers, glasses, etc.). In such cases, the ability to more reliably decongest the contributions of the nanotubes and the other material could be quite advantageous. In addition, surface induced doping can readily be seen, e.g. by a good fit of the S_{11} region and an underestimation of the S_{22} region. Another use, that pertains particularly to photovoltaics or light emitting devices wherein the nanotubes are (one of) the core light absorbing/emitting element(s), is in the calculation of quantum efficiency. For example, in our previous work we showed that it is possible to derive the (n,m)-resolved internal quantum efficiency of

nanotubes in SWCNT/Fullerene-C_{60} solar cells even when there is very significant overlap in the spectra of both the optical absorption and the photocurrent.[1]

Variation of relative concentration change of (n,m) distribution for the fit of film absorption spectra

Table S3. Comparison of relative concentration of different (n,m) species in solution (left column) and film (right column) for different film absorption background subtractions and different concentration constraints (x_i).

	Spectral Weight (%)					
Background / SWCNT	Fano + Lorentzian ($x_i = \pm 10$ %)		k / λ^b ($x_i = \pm 100$ %)		$A \cdot e^{-\lambda \cdot b}$ ($x_i = \pm 100$ %)	
(7,6)	25.89	25.37	25.89	24.60	25.89	26.26
(8,6)	24.08	22.92	24.08	22.76	24.08	21.68
(9,5)	16.50	17.66	16.50	17.03	16.50	16.97
(7,5)	5.54	4.92	5.54	3.57	5.54	2.71
(10,2)	1.04	0.92	1.04	0.412	1.04	0.17
(8,3)	0.22	0.23	0.22	0.14	0.22	0.15
(9,1)	0.60	0.65	0.60	0.01	0.60	0.04
(6,5)	1.19	1.11	1.19	1.29	1.19	0.89
(9,4)	1.22	1.19	1.22	1.28	1.22	0.77
(8,4)	1.71	1.72	1.71	1.46	1.71	1.06
(9,2)	5.13	5.12	5.13	7.06	5.13	5.08
(8,7)	10.83	11.66	10.83	12.24	10.83	12.98
(9,7)	4.22	4.55	4.22	4.87	4.22	7.65
(10,6)	1.83	1.97	1.83	3.28	1.83	3.60

Variables used during fitting

Table S4. List of all variables used during solution fitting.

Variable	Lower Limit	Starting Value	Upper Limit
Shift of center for any (n,m) species not assigned to a peak by the user (nm)	-5	0	20
Shift of center for any (n,m) assigned to a peak by the user (nm)	-5	0	5
Broadening of FWHM	0.8	1	1.3
Height guess	-	Method 1	-
Factor times most intense peak	0.8	0.95	1
Factor times height for Method 1	0.1	0.9	1
Factor times height for Method 2	0.1	1	1.2
Starting FWHM of Lorentzian for calculation of Voigitan FWHM (nm)	-	40	-
Ratio of Gaussian to Lorentzian FWHM for calculation of Voigtian FWHM	0.1	1	2
Change of ratio of Gaussian to Lorentzian FWHM	0.8	1	1.2
Cuvette path length for calculation of absolute concentration (cm)	-	0.2	-
Starting value for FWHM of Gaussian EPS (nm)	-	40	-
Broadening of initial FWHM of Gaussian EPS (nm)	0.5	1	2
Change of FWHM within different EPSs	0.9	1	1.1
Shift of EPS center position (eV)	-0.005	0	0.005
f_1 (in eq S33)	-0.07	0	0.07
Height ratio of S_{11}/S_{22}	1	4	5
Change of height within height ratios	0.8	1	1.2
Change of S_{22} height upon addition of metallic nanotubes	0.85	0.9	1.05
Change of S_{22} FWHM upon addition of metallic nanotubes	0.75	0.8	1.05
Change of EPS FWHM in S_{22} upon addition of metallic nanotubes	0.95	1	1.05
Change of EPS f_1 in S_{22} upon addition of metallic nanotubes	0.95	1	1.05
Change of ratio of Gaussian to Lorentzian FWHM upon addition of metallic nanotubes	0.95	1	1.05
Shift of metallic nanotube center position (nm)	-5	0	20
Broadening of initial FWHM for metallic nanotubes	0.6	1	1.3
Change of height for metallic nanotubes	0.1	1.2	1.6

Table S5. List of all variables used during film fitting

Variable	Lower Limit	Starting Value	Upper Limit
Shift of center position (nm)	0	30	40
Concentration change ± (%)		10	
Broadening of FWHM	0.5	2	2.5
f_1 (in eq S33)	-0.05	0	0.1
Broadening of initial FWHM of Gaussian EPS (nm)	1	2	3
Consider surface doping?		Yes	

References

1. Pfohl, M.; Glaser, K.; Graf, A.; Mertens, A.; Tune, D. D.; Puerckhauer, T.; Alam, A.; Wei, L.; Chen, Y.; Zaumseil, J.; Colsmann, A.; Krupke, R.; Flavel, B. S., Probing the Diameter Limit of Single Walled Carbon Nanotubes in SWCNT: Fullerene Solar Cells. *Advanced Energy Materials* **2016**, 1600890.
2. Bachilo, S. M.; Strano, M. S.; Kittrell, C.; Hauge, R. H.; Smalley, R. E.; Weisman, R. B., Structure-Assigned Optical Spectra of Single-Walled Carbon Nanotubes. *Science* **2002,** *298* (5602), 2361-2366.
3. Cambré, S.; Wenseleers, W., Separation and Diameter-Sorting of Empty (End-Capped) and Water-Filled (Open) Carbon Nanotubes by Density Gradient Ultracentrifugation. *Angewandte Chemie International Edition* **2011,** *50* (12), 2764-2768.
4. Papula, L., Fourier-Transformationen. In *Mathematische Formelsammlung: Für Ingenieure und Naturwissenschaftler*, Springer Fachmedien Wiesbaden: Wiesbaden, 2014; pp 311-338.
5. Nair, N.; Usrey, M. L.; Kim, W.-J.; Braatz, R. D.; Strano, M. S., Estimation of the (n,m) Concentration Distribution of Single-Walled Carbon Nanotubes from Photoabsorption Spectra. *Analytical Chemistry* **2006,** *78* (22), 7689-7696.
6. Olivero, J. J.; Longbothum, R. L., Empirical fits to the Voigt line width: A brief review. *Journal of Quantitative Spectroscopy and Radiative Transfer* **1977,** *17* (2), 233-236.
7. Schreier, F., Optimized implementations of rational approximations for the Voigt and complex error function. *Journal of Quantitative Spectroscopy and Radiative Transfer* **2011,** *112* (6), 1010-1025.
8. Weisman, R. B.; Bachilo, S. M., Dependence of Optical Transition Energies on Structure for Single-Walled Carbon Nanotubes in Aqueous Suspension: An Empirical Kataura Plot. *Nano letters* **2003,** *3* (9), 1235-1238.
9. Crochet, J. J.; Sau, J. D.; Duque, J. G.; Doorn, S. K.; Cohen, M. L., Electrodynamic and Excitonic Intertube Interactions in Semiconducting Carbon Nanotube Aggregates. *ACS Nano* **2011,** *5* (4), 2611-2618.
10. Wang, F.; Sfeir, M. Y.; Huang, L.; Huang, X. M. H.; Wu, Y.; Kim, J.; Hone, J.; O'Brien, S.; Brus, L. E.; Heinz, T. F., Interactions between Individual Carbon Nanotubes Studied by Rayleigh Scattering Spectroscopy. *Physical Review Letters* **2006,** *96* (16), 167401.
11. Perebeinos, V.; Tersoff, J.; Avouris, P., Effect of exciton-phonon coupling in the calculated optical absorption of carbon nanotubes. *Physical review letters* **2005,** *94* (2), 027402.
12. Kadria-Vili, Y.; Bachilo, S. M.; Blackburn, J. L.; Weisman, R. B., Photoluminescence Side Band Spectroscopy of Individual Single-Walled Carbon Nanotubes. *The Journal of Physical Chemistry C* **2016,** *120* (41), 23898-23904.
13. Liu, K.; Hong, X.; Choi, S.; Jin, C.; Capaz, R. B.; Kim, J.; Wang, W.; Bai, X.; Louie, S. G.; Wang, E.; Wang, F., Systematic determination of absolute absorption cross-section of individual carbon nanotubes. *Proceedings of the National Academy of Sciences* **2014,** *111* (21), 7564-7569.
14. Naumov, A. V.; Ghosh, S.; Tsyboulski, D. A.; Bachilo, S. M.; Weisman, R. B., Analyzing Absorption Backgrounds in Single-Walled Carbon Nanotube Spectra. *ACS Nano* **2011,** *5* (3), 1639-1648.
15. Sanchez, S. R.; Bachilo, S. M.; Kadria-Vili, Y.; Lin, C.-W.; Weisman, R. B., (n,m)-Specific Absorption Cross Sections of Single-Walled Carbon Nanotubes Measured by Variance Spectroscopy. *Nano letters* **2016,** *16* (11), 6903-6909.

16. Jain, R. M.; Howden, R.; Tvrdy, K.; Shimizu, S.; Hilmer, A. J.; McNicholas, T. P.; Gleason, K. K.; Strano, M. S., Polymer-free near-infrared photovoltaics with single chirality (6,5) semiconducting carbon nanotube active layers. *Advanced materials* **2012,** *24* (32), 4436-9.
17. Pfohl, M.; Glaser, K.; Ludwig, J.; Tune, D. D.; Dehm, S.; Kayser, C.; Colsmann, A.; Krupke, R.; Flavel, B. S., Performance Enhancement of Polymer-Free Carbon Nanotube Solar Cells via Transfer Matrix Modeling. *Advanced Energy Materials* **2016,** *6* (1), 1501345.
18. Berciaud, S.; Cognet, L.; Poulin, P.; Weisman, R. B.; Lounis, B., Absorption Spectroscopy of Individual Single-Walled Carbon Nanotubes. *Nano letters* **2007,** *7* (5), 1203-1207.
19. Tian, Y.; Jiang, H.; Anoshkin, I. V.; Kauppinen, L. J. I.; Mustonen, K.; Nasibulin, A. G.; Kauppinen, E. I., A reference material of single-walled carbon nanotubes: quantitative chirality assessment using optical absorption spectroscopy. *RSC Advances* **2015,** *5* (125), 102974-102980.
20. Tian, Y.; Jiang, H.; Pfaler, J. v.; Zhu, Z.; Nasibulin, A. G.; Nikitin, T.; Aitchison, B.; Khriachtchev, L.; Brown, D. P.; Kauppinen, E. I., Analysis of the Size Distribution of Single-Walled Carbon Nanotubes Using Optical Absorption Spectroscopy. *The Journal of Physical Chemistry Letters* **2010,** *1* (7), 1143-1148.
21. Ferguson, A. J.; Dowgiallo, A.-M.; Bindl, D. J.; Mistry, K. S.; Reid, O. G.; Kopidakis, N.; Arnold, M. S.; Blackburn, J. L., Trap-limited carrier recombination in single-walled carbon nanotube heterojunctions with fullerene acceptor layers. *Physical Review B* **2015,** *91* (24), 245311.
22. Meier, R. J., On art and science in curve-fitting vibrational spectra. *Vibrational Spectroscopy* **2005,** *39* (2), 266-269.